Journal of Biomedical Optics

BiomedicalOptics.SPIEDigitalLibrary.org

Extracting morphometric information from rat sciatic nerve using optical coherence tomography

James Hope
Bastian Braeuer
Satya Amirapu
Andrew McDaid
Frédérique Vanholsbeeck

SPIE.

James Hope, Bastian Braeuer, Satya Amirapu, Andrew McDaid, Frédérique Vanholsbeeck, "Extracting morphometric information from rat sciatic nerve using optical coherence tomography," *J. Biomed. Opt.* **23**(11), 116001 (2018), doi: 10.1117/1.JBO.23.11.116001.

Extracting morphometric information from rat sciatic nerve using optical coherence tomography

James Hope,[a,b,*] Bastian Braeuer,[a,d] Satya Amirapu,[c] Andrew McDaid,[b] and Frédérique Vanholsbeeck[a,d,*]
[a]The Dodd Walls Centre for Photonic and Quantum Technologies, New Zealand
[b]University of Auckland, Department of Mechanical Engineering, Auckland, New Zealand
[c]University of Auckland, Anatomy and Medical Imaging, Auckland, New Zealand
[d]University of Auckland, Department of Physics, Auckland, New Zealand

Abstract. We apply three optical coherence tomography (OCT) image analysis techniques to extract morphometric information from OCT images obtained on peripheral nerves of rat. The accuracy of each technique is evaluated against histological measurements accurate to $+/-1$ μm. The three OCT techniques are: (1) average depth-resolved profile (ADRP), (2) autoregressive spectral estimation (AR-SE), and (3) correlation of the derivative spectral estimation (CoD-SE). We introduce a scanning window to the ADRP technique, which provides transverse resolution and improves epineurium thickness estimates—with the number of analyzed images showing agreement with histology increasing from 2/10 to 5/10 (Kruskal–Wallis test, $\alpha = 0.05$). A method of estimating epineurium thickness, using the AR-SE technique, showed agreement with histology in 6/10 analyzed images (Kruskal–Wallis test, $\alpha = 0.05$). Using a tissue sample in which histology identified two fascicles with an estimated difference in mean fiber diameter of 4 μm, the AR-SE and CoD-SE techniques both correctly identified the fascicle with larger fiber diameter distribution but incorrectly estimated the magnitude of this difference as 0.5 μm. The ability of the OCT signal analysis techniques to extract accurate morphometric details from peripheral nerves is promising but restricted in depth by scattering in adipose and neural tissues. [DOI: 10.1117/1.JBO.23.11.116001]

Keywords: optical coherence tomography; medical and biomedical imaging; neurology; bio-photonics.

Paper 180249R received May 1, 2018; accepted for publication Oct. 15, 2018; published online Nov. 3, 2018.

1 Introduction

In the field of neural prosthetics, the performance of nerve cuffs for recording and stimulating bioelectric signals can be improved using physiologically accurate volume conductor models of nerves.[1,2] The morphometric details required for such models are the size, number, and location of fascicles, the thickness of the epineurium and perineurium ultrastructural tissue layers, and the spatial variations in fiber diameter distribution. It is common to use simplified morphometric details, such as in Refs. 2–4; however, the results are not transferrable to patients due to patient-specific tissue morphology. Another approach is to use destructive imaging methods, such as light microscopy, to acquire micrometer resolution histological images of the nerve cross section at one location and then extrude this along the length dimension, such as in Refs. 5 and 6; however, this does not account for the length variation in tissue morphology caused by fascicle bifurcation.[7] Magnetic resonance imaging (MRI) enhanced with gadolinium-DTPA (diethylenetriamine penta-acetic acid) contrast agent, a nondestructive imaging method, has been used to image the size, number, and location of fascicles in an extracted nerve tissue with a voxel size of $30 \times 30 \times 250$ μm^3,[1] which is promising, particularly if replicated with *in vivo* measurements. For a patient-specific and physiologically accurate model, a nondestructive volumetric imaging method is required with a resolution of several μm.

The structure of peripheral nerves comprises one or more fascicles bound together by epineurium tissue, 10's of μm thick.[8] In humans, the median nerve is several mm across and can contain 10 or more fascicles at the elbow, with each fascicle ranging in size from 0.12 to 2 mm^2,[9] whereas, in comparison, the rat sciatic nerve is approximately 1 mm across and can contain 3 to 4 fascicles ranging in size from 0.05 to 1 mm^2. Each fascicle contains several thousand nerve fibers bound together by endoneurium tissue, and encompassed by a layer of perineurium tissue several μm thick.[10] Nerve fibers are long cylinders ranging in size from 1- to 22-μm diameter and are heterogeneously distributed within fascicles;[9] they are also highly aligned, densely packed, and usually sheathed in a lipid-rich myelin from encasing Schwann cells. The orders of magnitude of the dimensions of the nerves under study place optical coherence tomography (OCT), a nondestructive imaging method, well as a potential means to acquire morphometric details without damaging the nerve.

Qualitative OCT techniques of distinguishing neural tissue from surrounding tissue,[11–14] identifying different neural tissue layers,[11–13,15,16] and analyzing levels of myelination[17] do not provide quantified values nor confidence levels. On the other hand, quantitative OCT techniques, such as the depth-resolved analysis of optical properties[18] and statistical analysis of spectra,[19,20] provide quantified values for nerve tissue morphometry but have not been validated. Other quantitative OCT techniques, such as the analysis of Mie scatter spectra[21] and optical scattering properties,[22] have been used to classify tissue, but have not yet been applied to peripheral nerves. There is, therefore, a need to evaluate and validate the performance of OCT techniques in imaging peripheral nerves, which builds on preliminary work in Ref. 23.

In this paper, we present results from three quantitative OCT signal analysis techniques that we identified in the literature and

*Address all correspondence to: James Hope, E-mail: jhop030@aucklanduni.ac.nz; Frédérique Vanholsbeeck, E-mail: f.vanholsbeeck@auckland.ac.nz

replicated with some improvements on images of rat sciatic nerve acquired with a swept source OCT (SS-OCT) system. Of the three OCT techniques—average depth-resolved profile (ADRP), autoregressive spectral estimation (AR-SE), and correlation of the derivative spectral estimation (CoD-SE)—one, the former, was selected for the current study as it was developed specifically for the estimation of the thickness of the external layer of epineurium. The identification and quantification of internal epineurium tissue layers would allow determination of the size, number, and location of fascicles. The latter two techniques, AR-SE and CoD-SE, were developed for scatter size estimation applications, and selected for the current study due to their potential to evaluate the spatial variations in fiber diameter distribution. With each technique, we attempt two tasks: (1) extract the epineurium layer thickness and (2) distinguish adipose tissue. In addition to this, for the two techniques based on scatter size estimation we attempt a third task. (3) Estimation of fiber diameter distribution of nerve fibers within fascicles. We compare our results with the histological analysis performed on light-microscopy images, a step that is absent in the original reporting of the OCT techniques.[18–21,24] When replicating each technique, parameters were selected using unbiased methods, or otherwise noted as biased, to ensure fair comparison and practical application. We demonstrate applications of the two scatterer size estimation techniques using them to evaluate the combined thickness of epineurium and perineurium tissue, and to differentiate adipose tissue from neural tissues. The results help to establish the abilities and limitation of current OCT techniques, and potential for OCT-based scatterer diameter estimation techniques, in extracting morphometric details from peripheral nerves, and demonstrates OCT as a complimentary tool for developing patient-specific nerve models to improve performance of neural prosthetics.

2 Materials and Methods

2.1 *Tissue Preparation and Handling*

The animal procedures were approved by the University of Auckland Animal Ethics Advisory Committee. All animal specimens were rats of Wistar breed and male. Euthanasia was performed by first anaesthetising with isoflurane and then performing cervical dislocation. A total of three nerve tissue samples were explanted, each extending the entire length of the sciatic nerve and, distal to bifurcation, as much of the tibial and peroneal branches as practicable. Samples were then stored in 0.01 M phosphate buffered solution (PBS) at 4°C for up to three days before being transported and imaged using OCT. The physiological pH and osmolarity of PBS ensured that the cellular and ultrastructural features of the sample were preserved. Several points along each tissue sample were randomly selected and marked with Davidson's marking dye and 1% picric acid, and these points imaged with OCT. *Ex vivo* imaging allowed any location of the nerve to be imaged by manipulating the nerve instead of the incident light beam, which would have required significant modifications to the OCT system. In this study, we present results and images from one point each from the sciatic section of two nerves, and one point from the tibial section of one nerve.

During OCT imaging, tissue samples were suspended at two points 20 mm apart along the length. Sagging of the tissue sample was used as a visual indication that the tissue sample was not mechanically stretched. Four OCT images, at 90-deg offsets, were acquired of the dyed points within the suspended section. Between image acquisitions, 0.01 M phosphate buffered solution was applied to the outside of the nerve, using a syringe to avoid tissue drying. Postimaging, the tissue samples were returned to the phosphate buffered solution and transported to the Anatomy and Medical Imaging department at the University of Auckland for histological analysis using light microscopy.

Error introduced by thermal expansion, caused by variation in the sample temperature during imaging between 4°C and 20°C, is expected to be <0.5% using the thermal expansion coefficient of water. Error introduced from stretching, due to suspension of the tissue samples during OCT imaging, is <0.05% using a Poisson's ratio and Young's modulus of 0.37 and 41 MPa, respectively.[25]

2.2 *Microsphere Samples*

Three microsphere samples (Spherotech Inc.) were used in this study with concentration, and mean diameter $+/-1$ standard deviation of: (1) 5% w/v, $3.8 +/- 0.25$ μm; (2) 5% w/v, $5.33 +/- 0.25$ μm; and (3) 2.5% w/v $8.49 +/- 0.25$ μm. Standard deviations of their respective size distributions were calculated using measured data provided by the supplier with the samples. For each sample, the vial containing the microspheres in the solution was shaken vigorously to ensure homogeneity of the solution before a 1-mL sample was extracted and transported, using a pipette, to a separate container under the OCT system and immediately imaged.

2.3 *Optical Coherence Tomography Image Acquisition and Processing*

The OCT system has a swept source centered at 1310 nm with an 80-nm bandwidth (3 dB). The system has 12.5-μm axial resolution, 20-μm lateral resolution, and the 6-dB drop off in air is over 12 mm. More details of the OCT system can be found in Refs. 26 and 27.

The B-scan direction was perpendicular to the length of the nerve tissue samples, spanned a physical distance of 5 mm, and contained 714 A-scans. B-scans were saved from the LABVIEW® user interface to text files and then processed individually with MATLAB® 2015b using the signal analysis techniques described below.

To determine the distance when calculating epineurium thickness, an average refractive index had to be used for the entire OCT image; here, we have used the refractive index of $n = 1.40$, which is the average of values reported for myelin (1.455)[28] and bovine tendon, a collagenous connective tissue, (1.353).[29] The axial distance per pixel, of 10 μm in air, was, therefore, 7.1 μm in neural tissues in all subsequent calculations of epineurium thickness.

2.4 *Histological Analysis by Light Microscopy*

Histology by light microscopy was performed at one location on each of the tissue samples, see Fig. 1. Tissue samples were preserved in 10% neutral buffered formalin for 24 hours, followed by 70% ethanol prior to paraffin embedding. Tissue slices of 10-μm thick were obtained using a microtome then hemotoxylin and eosin were used to stain the collagen-rich epineurium, perineurium, and endoneurium tissues pink. The lipid-rich myelin was stained with Luxol Fast Blue. Images were obtained on a Leica DM500 light microscope at 4×, 10×, and 40×

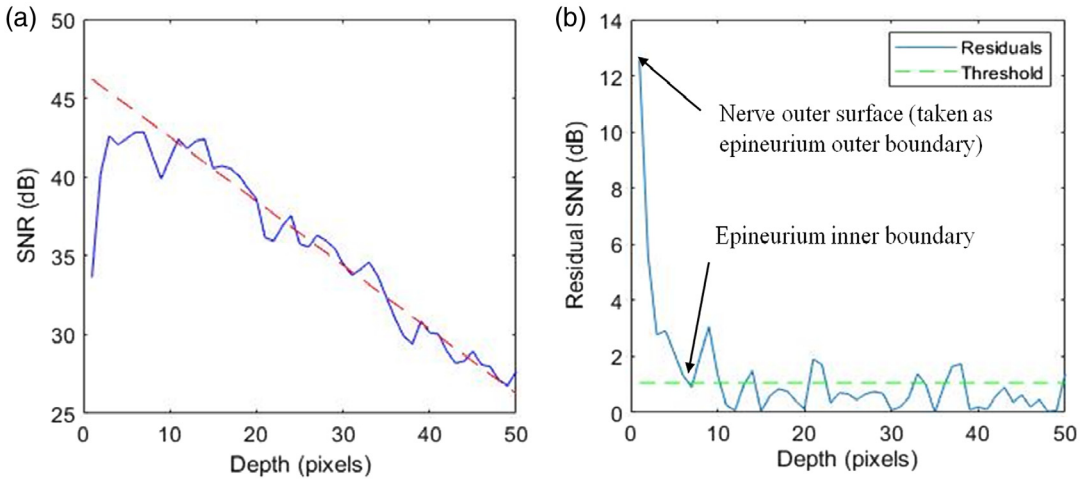

Fig. 1 An ADRP curve generated by averaging five adjacent A-scans from a flattened OCT image and the linear fit calculated from pixel depth range of 15 to 50 pixels (a), where a pixel depth of 0 is the surface. The residuals, calculated from Fig. 1(a), and the threshold line used to determine the epineurium inner boundary (b).

magnifications. A uniform shrinkage of 10%, produced during the preparation process, was taken into account by multiplying all values extracted from histology by a factor of 1.1.

The thickness of epineurium tissues was determined using images obtained at 4× magnification. In each image, a line was drawn through the tissue layers, perpendicular to the tissue outer surface, at 20 locations approximately equidistant around the fascicle boundaries. Then, the thickness of tissue along these lines was measured manually. Error introduced by the measurement procedure was estimated to be $+/-1$ μm.

Fiber diameter distribution was calculated in areas of the tissue sample images that were visually identified as containing a few artifacts from sample preparation. A grid of 100-μm squares was laid over the area of interest in the 40× magnification images and the fiber diameter distribution was calculated for each grid square. Fibers were typically ellipsoid shaped; therefore, the major and minor axes were used to calculate the diameter of a circle with an equivalent area. The diameter estimates contained $\sim+/-1$ μm uncertainty. Furthermore, the method employed could not identify fiber diameters <3 μm due to the very thin, or absent in the case of unmyelinated fibers, myelin sheath.

2.5 *Average Depth-Resolved Profile Technique*

Two techniques to identify the fascicle boundary, one using structural data and the other phase retardation data, are presented in Ref. 18. Both techniques are applied to the ADRP of the middle 50% of A-scans of the tissue sample. The ADRP is generated by first cropping pixels outside the tissue sample, then flattening the remaining pixels so that each row in the columns of data (A-scan) correlates to the same axial depth in the tissue sample, and, finally, averaging values across each row. To estimate the fascicle boundary with higher lateral resolution, we implemented the ADRP across windows containing five A-scans, which were scanned laterally across the sample in one-pixel steps.

The ADRP-structural-data technique operates on the expectation that the anatomy of the intrafascicle volume will produce a uniform decay rate of the OCT signal.[18] To identify the fascicle boundary, the ADRP-structural-data technique plots the signal-to-noise ratio (SNR) of the ADRP on a logarithmic scale against depth, then fits a linear slope to the uniformly decaying region of the curve, Fig. 1. The absolute difference between the linear fit and the ADRP curve forms the residual SNR curve. A threshold value is then calculated as the mean plus 2 standard deviations from the linear portion of the residual SNR curve. The fascicle boundary is identified by the intersection of the threshold value and the curve neighboring the uniformly decaying region. In our implementation of the five A-scans sliding window method, we fit the linear slope to data from a depth range of 15 to 50 pixels in all window ADRPs, Fig. 1. The start value of 15 pixels correlates to a depth of 113 μm, which is outside the typical epineurium thickness values provided by histological analysis and, therefore, is highly unlikely to include epineurium tissue.

We calculated the SNR at each depth using $\mathrm{SNR} = 20\log(I/\sigma)$, where I is the signal intensity at that depth, and σ is the standard deviation of the noise. To find σ, we determined the standard deviations of the five A-scans nearest to one end of the B-scan, and so known not to contain any reflectors across the depth range of interest, and then calculated the average of these standard deviations.

To identify adipose tissue, we calculated the threshold from the entire portion of the residual SNR curve, instead of just the linear portion, which increases the threshold value. In areas with epineurium, the residual-SNR curve in the uniformly decaying region was below the threshold and the initial peaks of the residual-SNR curve, associated with epineurium, were above the threshold. Conversely, in areas with adipose tissue, which contained multiple peaks and no uniformly decaying region, the residual SNR curve oscillated around the threshold.

In the ADRP-phase-retardation technique, a linear slope is fitted to the rising portion in a plot of phase retardation against depth, which occurs due to the birefringence of myelin. The residuals, threshold, and fascicle boundary are then calculated in the same way as the ADRP-structural-data technique. We did not employ the ADRP phase-retardation technique on any tissue samples as our system was not polarization sensitive.

2.6 *Autoregressive Spectral Estimation Technique*

The diameter range of nerve fibers places them in the Mie scattering regime, which generates diameter-dependent spectral

modifications. The AR-SE technique for estimating scatterer diameter, which statistically analyses the spectral content of backscattered light, was originally presented in Ref. 30 and then applied to biological samples, including the sciatic nerve of rabbit, in Refs. 19 and 20. The technique assumes a linear relationship between the scatterer diameter $\tilde{\mathbf{d}}$ and the eigenvectors produced by principal component analysis (PCA) of the power spectral density $\widetilde{\mathbf{P}_{xx}}$ produced using the Burg's method, such that $\widetilde{\mathbf{P}_{xx}}\,\tilde{\mathbf{A}} = \tilde{\mathbf{d}}$ where $\tilde{\mathbf{A}}$ is a coefficient matrix that is populated using samples of known diameter, also called "training data."

To obtain the training data, we used the three microsphere samples described above (Sec. 2.2). A window of 50×10 pixels (axial × transverse) in size was raster scanned across half of the OCT image at 25 and 1 pixel steps, respectively. Data were row-averaged to suppress noise and normalized to reduce variations from depth attenuation. The decay of autoregressive reflection coefficients toward zero determined the autoregressive order to use in calculating the power spectral density. A target variance of 99.99% determined the number of components to extract from weighted PCA of the power spectral density data. The remaining half of each OCT image of microspheres was used to obtain diameter estimates.

In applying the AR-SE technique to OCT data from tissue samples, larger window sizes reduce noise, but potentially remove more of the targeted detail such as the intrafascicle boundary and localized variation in fiber diameter distribution. Furthermore, the maximum autoregressive order that can be applied is one less than the number of data points, i.e., the axial window size. A window size of 10×10 pixels, scanned at 1 pixel steps, was selected as it produced a good balance between noise reduction and sufficient resolution. At each step, the autoregressive order to use was determined by analyzing the autoregressive reflection coefficients, with a drop below $+/-0.2$ in magnitude used as the threshold criterion. Alternatively, when the decay of autoregressive reflection coefficients toward zero was not clearly identifiable, an autoregressive order of 3 was selected as this value was common in the tissue samples and was found to minimize noise in the solution.

In the processed OCT images, each lateral and depth pixel contained a fiber diameter estimate. An area of interest was selected from the processed OCT images, which began sufficiently below the surface to pertain to the intrafascicle volume, and the diameter estimates at all pixels within the area formed the sample for the analysis of fiber diameter distribution.

2.7 *Correlation of the Derivative Spectral Estimation Technique*

The CoD-SE technique was originally presented in Ref. 24, and then again with additional signal processing steps in Ref. 21. This technique uses Mie theory to generate spectra for spherical scatterers before taking the derivative and then the autocorrelation to produce the CoD. The CoD bandwidth is calculated as the first minimum, i.e., the minimum with the lowest lag value, in the CoD of the spectra. A curve is fitted to a plot of the theoretical relationship between the scatterer diameter and CoD bandwidth. In OCT data, the spectra are obtained using the Fourier transform with a Gaussian window. To lower the noise, spectra are low-pass filtered and the edges are removed. Differentiating with respect to the neighboring value followed by autocorrelation produces the CoD. CoD-SE is highly sensitive to the lateral position of the window relative to the scatterer, and to the axial window size. To address the former, an intensity threshold of 5 dB above the noise level is introduced and the highest intensity of three laterally adjacent windows is assigned to all three lateral positions. To address the latter, the axial window size, which is used to obtain sample spectra, is selected to minimize the standard deviation of the resulting scatterer diameter estimates.

We appended an additional step to the end of the original method, outlined in the previous paragraph to improve the scatterer diameter estimates produced from our microsphere samples: the window axial size was selected to minimize the "normalized" standard deviation of the scatterer diameter estimate, calculated as the standard deviation divided by the corresponding mean.

The CoD-SE algorithm was tested on three microsphere samples with same concentration and mean diameter as in the AR-SE experiments, see Sec. 2.5. We generated the theoretical curve using the MATLAB functions of Mie theory presented in Refs. 31 and 32 and refractive indices of water and polystyrene[33] ($n_{\text{water}} = 1.3225 + 0.001i$ and $n_{\text{poly}} = 1.59 + 0.0025i$). We then fitted an exponential function of the form $f_{\text{CoD}} = d^A e^B$, where f_{CoD} is the CoD bandwidth, d is the diameter, and A and B are constants defining the curve, as this provided an excellent fit within the diameter range from 3 to 16 μm. Unbiased methods were not identified to select (1) the standard deviation of the Gaussian window in the Fourier transform and (2) the extent to crop the edges of spectra to remove noise. A standard deviation of the Gaussian window equal to half of the window size, and cropping of 3.9 nm (100/4096 points) from each end of the spectral range were selected through trial and error using the microsphere samples. Diameter estimates were produced for each image pixel using 13 different axial window sizes from 3 to 15 pixels, all with a lateral size of 1 pixel, scanned at 1 pixel steps. At each step, and for each window size, the Butterworth filter (second order, zero phase, low pass) cut-off frequency was selected using Winter's method, with resulting values in the range of $0.225 +/- 0.004$ π.rad/sample ($0.899 +/- 0.016$ nm^{-1}).

For tissue samples, we could not find a value for the refractive index of endoneurium nor its close relative epineurium. Instead, we used bovine tendon, which is, like endoneurium, a collagen-rich connective tissue. Therefore, we generated the theoretical CoD bandwidth curve using refractive indices of myelin ($n_{\text{myelin}} = 1.455$[28]) and bovine tendon ($n_{\text{tendon}} = 1.353$[29]), to which we fitted an exponential function of the form $f_{\text{CoD}} = d^A e^B$. Values for the standard deviation of the Gaussian window in the Fourier transform, the extent to crop the edges of spectra, and the Butterworth filter parameters were all carried over from microsphere experiments. Axial window sizes from 3 to 15 pixels were used to generate diameter estimates, and then a 3×3 scanning window was used to determine the diameter estimate to use for each pixel location based on the minimization of the normalized standard deviation. Scatterer size estimates were directly assigned as fiber diameter distribution estimates.

In the processed OCT images, each lateral and depth pixels contained a fiber diameter estimate. An area of interest was selected from the processed OCT images, which encompassed the intrafascicle volume, and the diameter estimates at all pixels within the area formed the sample for analysis of fiber diameter distribution.

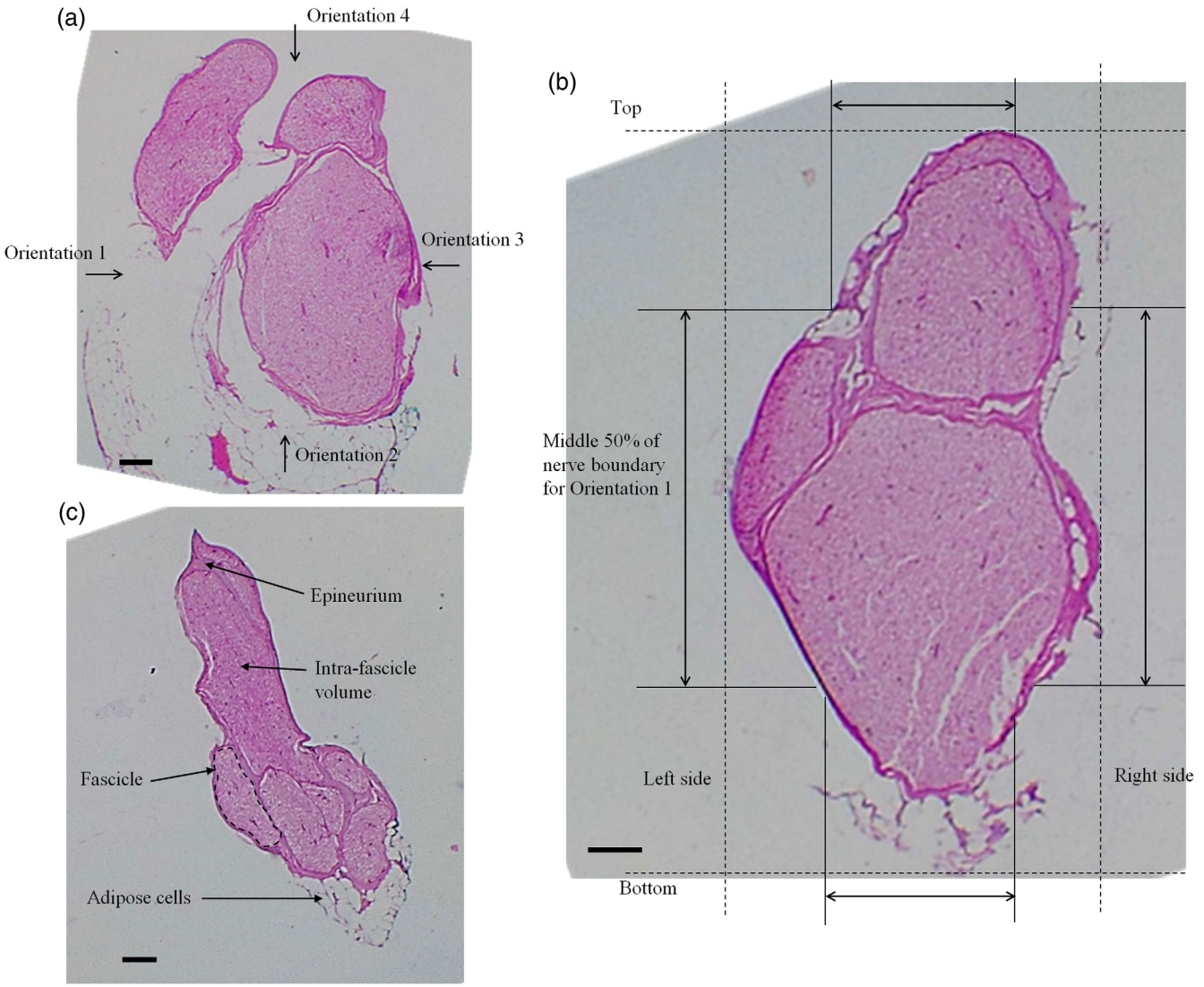

Fig. 2 Light microscopy images at 4× magnification, stained with H&E, of tissue sample 1 (a) and tissue sample 2 (b) of sciatic nerves, and tissue sample 3 (c) of the tibial nerve branch. In all images the scale bar is 100 μm. Images have been rotated in order that the incident beam in OCT, acquired for four tissue orientations, coincides with each side of the light microscopy image, where the sides: left, bottom, right, and top correspond to OCT imaging orientations: 1, 2, 3, and 4, respectively (a). After alignment with OCT, the top, bottom, and two sides of the nerve within each histological image were identified, shown with dashed lines in (b), and the middle 50% of the nerve boundary was assigned as the middle 50% in linear distance between the respective ends, shown with arrows in (b). Tissue features of peripheral nerve are labeled in (c).

3 Results

3.1 *Epineurium Thickness*

3.1.1 *Histological analysis*

With H&E staining of the fascicle, boundaries in the sciatic branches were clearly identifiable in light microscopy images of all three tissue samples, by the change from dark pink stained epineurium and perineurium tissues to the lighter pink intrafascicle environment mottled with unstained nerve fibers, Fig. 2. Adipose cells are unstained by H&E. Adipose tissue commonly appeared in clusters of several cells, each with a diameter of >20 μm, apposed to the nerve outer boundary in large quantities in tissue sample 1 and in small quantities in tissue samples 2 and 3, Fig. 2.

The combined epineurium and perineurium thickness was estimated at $50+/-38$ μm, $45+/-32$ μm, and $31+/-25$ μm (mean $+/-1$ standard deviation) across the entire light microscopy image for tissue samples 1, 2, and 3 respectively.

Due to the small thickness of perineurium relative to epineurium, and because one layer of each are always present and adjacent to one another in the tissue layer separating the intrafascicle volume and the outer nerve boundary, from here onward we refer to the combined epineurium and perineurium tissue layer as just the epineurium layer.

When the light microscopy images were aligned to the corresponding OCT images, and the middle 50% of the nerve boundary was analyzed to match the area imaged and analyzed by OCT, the localized standard deviations of the epineurium thickness estimates were smaller than those obtained for the entire

Table 1 Epineurium tissue layer thickness, in μm, estimated from histology, conventional and 5Ascan methods within the ADRP technique, and with a 10×10 window for the AR-SE technique. Mean (standard deviation). A refractive index of 1.41, producing 7.1-μm axial distance per pixel within nerve tissue, used to obtain ADRP and AR-SE values. Histology estimates are taken across the middle 50% of each orientation, whereas the ADRP and AR-SE signal analysis techniques are applied to the middle 50% of A-scans in each image. RS, right skewed; MM, multimodal. In the ADRP conventional column, bold indicates values within $+/-1$ standard deviation of the value obtained using light microscopy. Elsewhere, italic indicates agreement of medians (Wilcoxen rank sum test, $\alpha = 0.05$) and analysis of variance (Kruskal–Wallis test, $\alpha = 0.05$) with the corresponding data obtained using light microscopy.

	Light microscopy	ADRP: conventional	ADRP: five A-scan	AR-SE: 10×10
Tissue sample 1				
Orientation 1	[a]	77	40 (37)	70 (75)
Orientation 2	[a]	91	42 (39)	72 (50)
Orientation 3	59 (34) MM	**63**	*48 (28) RS*	27 (24) RS
Orientation 4	19 (10) RS	85	37 (27) RS	*17 (22) RS*
Tissue sample 2				
Orientation 1	28 (19) RS	83	44 (28) RS	*43 (50) RS*
Orientation 2	29 (11) RS	91	61 (32) MM	*22 (23) RS*
Orientation 3	44 (20) RS	91	*56 (34) MM*	*44 (41) RS*
Orientation 4	30 (25) RS	105	*33 (34) RS*	*26 (31) RS*
Tissue sample 3				
Orientation 1	23 (14) MM	77	57 (38) RS	43 (43) RS
Orientation 2	41 (29) MM	**46**	*28 (29) RS*	28 (39) RS
Orientation 3	22 (12) RS	71	*40 (37) RS*	20 (25) RS
Orientation 4	22 (16) RS	49	51 (35) RS	*27 (32) RS*

[a]Adipose tissue prevalent.

nerve. This indicates epineurium thickness varies along the outer boundary. The distribution of the thickness estimates for tissue sample 1 orientation 3 and tissue sample 3 orientations 1 and 2 showed multiple peaks across the range of values, i.e., multimodal. All other tissue samples' orientations were right skewed, i.e., favoring smaller thickness, see Table 1.

3.1.2 *Average depth-resolved profile techniques*

Using the conventional ADRP-structural-data method, to construct the ADRP from the middle 50% of A-scans, estimates of the combined epineurium thickness from all orientations of tissue samples 1 and 2 were consistently lower than results obtained from sciatic nerve presented in the original study for the ADRP-structural-data technique of $133 +/- 14$ μm.[18] Tissue sample 3 is from the tibial nerve branch and so is not directly comparable. Epineurium thickness estimates obtained using the conventional ADRP-structural-data technique on tissue sample 1 orientation 3 and tissue sample 2 orientation 2 are within $+1$ standard deviation, and tissue sample 3 orientation 4 within $+2$ standard deviations of the mean values provided by measurement from the corresponding histology by light microscopy. The remaining estimates are $> +2$ standard deviations, indicating significant disagreement between values as shown in Table 1.

Thickness estimates using the five A-scans sliding window method were consistently lower than those obtained using the conventional ADRP method. Furthermore, with the exception of tissue sample 2 orientations 2 and 3, the distribution of thickness estimates was right skewed, i.e., favoring smaller thickness. With the exception of tissue sample 2 orientation 2, all estimates in Table 1 obtained using the ADRP-5Ascan method are within 1 standard deviation of the values obtained from light microscopy; however, the right skewed distributions of data make means a poor measure for comparison. The medians (Wilcoxon rank sum test, $\alpha = 0.05$) and analysis of variance (Kruskal–Wallis test, $\alpha = 0.05$) of estimates obtained with the ADRP-5Ascan from tissue sample 1 orientation 3, tissue sample 2 orientations 3 and 4, and tissue sample 3 orientations 2 and 3 were in agreement with the corresponding histology by light microscopy.

3.1.3 *Autoregressive spectral estimation technique*

The layer of epineurium and perineurium tissues was visually identified as a contiguous area of large diameter scatterers along the surface of the nerve. The relationship between the thickness of this contiguous layer of scatterers and the thickness of the epineurium tissue was investigated using a digital phantom of an epineurium layer, which was constructed using a 50×50 element array with each element equal to 0.01 and within this array several adjacent rows containing values of 1 to mimic epineurium. Application of the AR-SE algorithm to the phantom showed the epineurium thickness along each

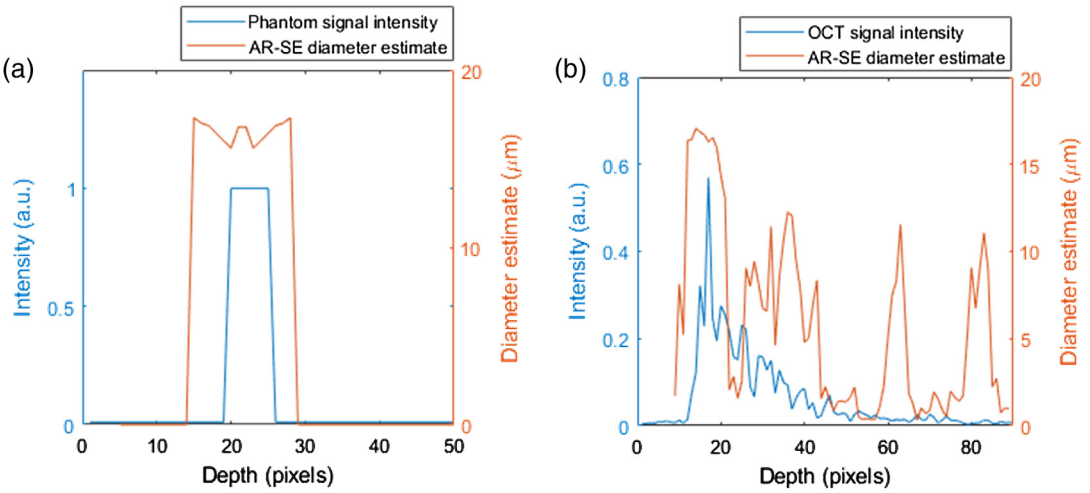

Fig. 3 Signal intensity and corresponding diameter estimate from the AR-SE algorithm for epineurium phantom (a) and an A-scan taken from tissue sample 1 orientation 4 (b). Using the phantom's response to the AR-SE algorithm it was determined that epineurium thickness can be estimated from the FWHM of the contiguous scatterer peak observed at the nerve outer boundary.

A-scan could be approximated by difference between the base width of the contiguous scatterer peak and the window axial size as shown in Fig. 3(a). In nerve samples, due to the presence of scatterers along the inside boundary of the epineurium tissue layer, Fig 3(b), we isolated the contiguous scatterer peak by removing scatterer estimates below 5 μm. We then subtracted the scanning window axial size from the full-width-half-mean of the contiguous scatterer peak, in place of the base width, to estimate the epineurium thickness.

Visual identification of the layer epineurium tissue, as a contiguous area of large diameter scatterers along the surface of the nerve, is an observation not reported in the original study. The distributions of thickness estimates produced with the AR-SE technique are generally right skewed with a long right-hand tail, which makes the means a poor measure for comparison, Fig. 4. Indeed, none of the AR-SE thickness estimate means were in agreement with their corresponding histology by light microscopy (two sample Kolmogorov–Smirnov test, $\alpha = 0.05$). Estimate medians (Wilcoxon rank sum test, $\alpha = 0.05$) and analysis of variance (Kruskal–Wallis test, $\alpha = 0.05$) of tissue sample 1 orientation 4, all orientations of tissue sample 2, and tissue sample 3 orientation 4 were in agreement with their corresponding histology by light microscopy.

It is evident in the box and whisker plots of AR-SE estimates in Fig. 4 that in all tissue samples and orientations there was at least one, and typically several, thickness estimates of 0 μm, which is biologically impossible.

3.1.4 *Correlation of the derivative spectral estimation technique*

Scatterer diameter estimates produced by the CoD-SE algorithm varied depending on the size of the square scanning window, with larger square windows favoring smaller mean diameter

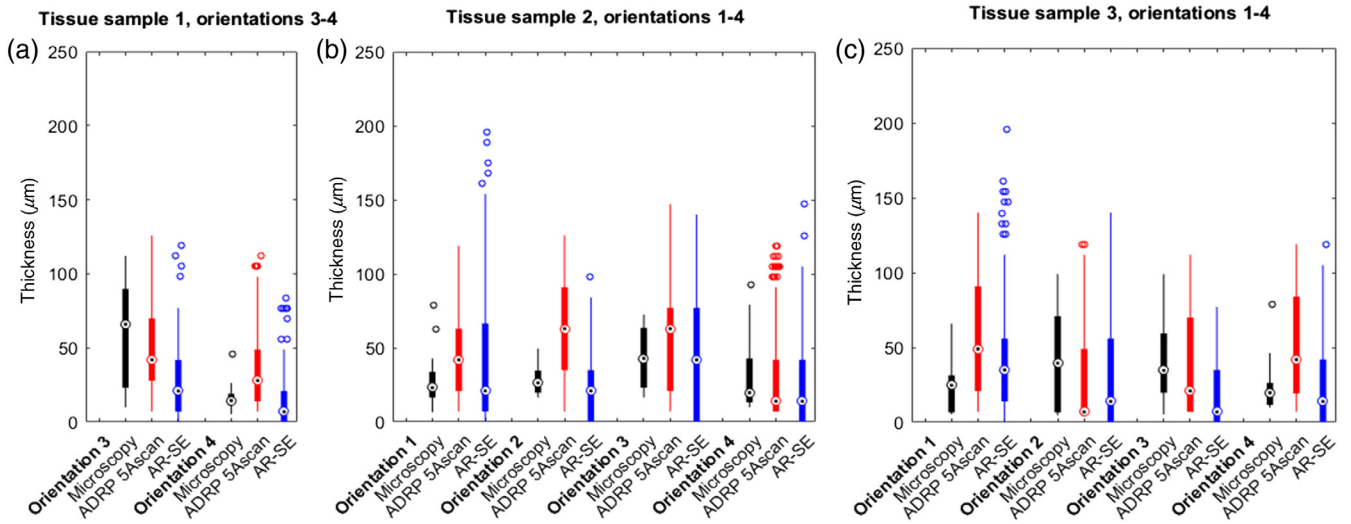

Fig. 4 Distribution of epineurium tissue layer thickness estimates for tissue samples (a) 1, (b) 2, and (c) 3. Within each tissue sample boxplot, estimates from histology by microscopy (black), the five A-scans window method within the ADRP technique (red), and AR-SE technique with a 10×10 window (blue), are grouped together for each orientation.

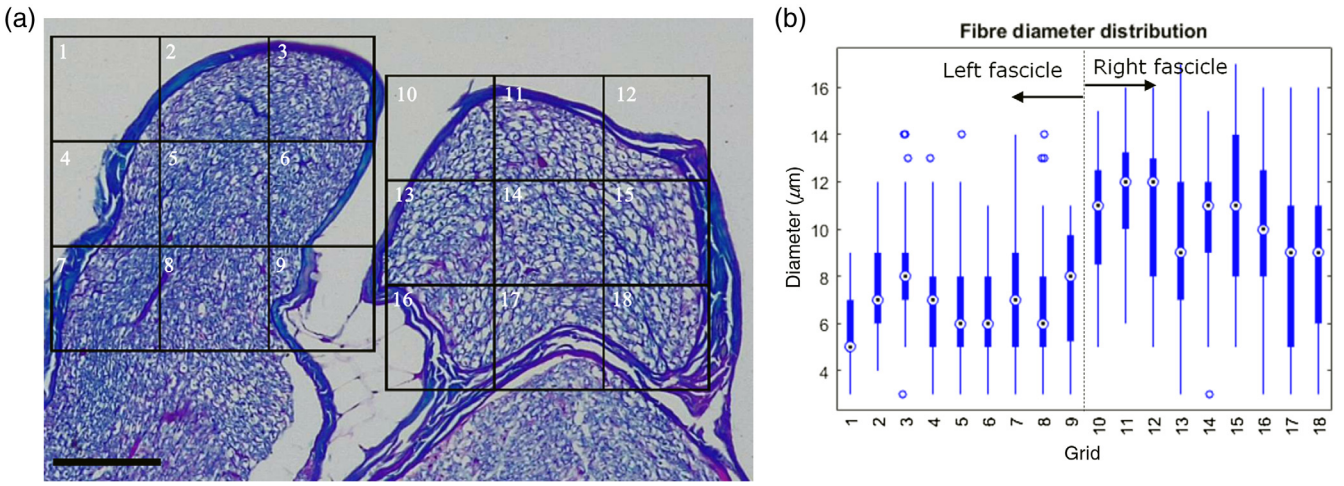

Fig. 5 Light-microscopy image of histology at 10× magnification of tissue sample stained with LF blue (a), scale bar is 100 μm. Numbered grid used in fiber diameter distribution calculations are shown overlaid on the light microscopy image (a), with results presented in box and whisker plots (b) confirming significant difference in fiber diameter distribution between the left (grids 1 to 9) and right (grids 10 to 18) fascicles.

estimates with smaller standard deviations. An unbiased method of selecting this parameter is desirable for practical application of the CoD algorithm. On OCT data of nerve tissue, a contiguous layer of estimates within the range of 2.2 to 4 μm were produced around the tissue boundary where the epineurium layer is expected to reside. Although this narrow diameter range may potentially provide a means to distinguish the epineurium layer from the adjacent air on one side and intrafascicle volume on the opposite side, we did not identify a method to easily isolate this layer from scatterers present along its internal and external boundaries. In addition, we did not extract a relationship between this contiguous layer and the epineurium thickness through the application of the CoD-SE algorithm to a digital phantom of an epineurium layer. Therefore, we did not pursue epineurium thickness estimation with the CoD-SE technique further.

3.2 *Fiber Diameter Distribution*

3.2.1 *Histological analysis*

Tissue sample 1 orientation 4 contained easily identifiable landmarks—in the form of two "humps"—for alignment to corresponding OCT images, and contained two fascicles with a difference in fiber diameter distributions that was easily perceptible at 10× and 40× magnifications, Fig. 5(a). Tissue sample 1 orientation 4 was therefore selected for fiber diameter distribution analysis. A minor histological artifact is evident in this sample where the left fascicle has been pulled away from the right fascicle during slicing on the microtome, box and whisker plots of the fiber diameter distributions within the left (grids 1 to 9) and right (grids 10 to 18) fascicles showed higher medians, upper and lower quartiles, and maximum values in the majority of grids in the right fascicle compared with grids of the left fascicle, Fig. 5(b). Further analysis, using a one-way ANOVA with $\alpha = 0.05$, revealed significant difference between the means of grids 1 and 3 within the left fascicle, and no significant difference between the means of grids in the right fascicle. The left and right fascicles possessed diameters of $6.1 + / - 2.1$ μm and $10.1 + / - 3.0$ μm (mean $+/-1$ standard deviation), respectively. A one-way ANOVA, $\alpha = 0.05$, also revealed significant difference in fiber diameter between the two fascicles, indicating a heterogeneous fiber diameter distribution at the fascicle level.

3.2.2 *Autoregressive spectral estimation technique*

In each of the microsphere samples, the autoregressive reflection coefficients decayed rapidly toward zero, Fig. 6(a), which specified low autoregressive orders for calculating the power spectral density. Weighted PCA of the power spectral densities produced similar, but distinguishable, eigenvectors for all three microsphere samples, Fig. 6(b), where, in all cases, the first variable contributed the most to the first two principal components, and the second variable contributed the most to the third principal component. The AR-SE technique estimated the diameters of microsphere samples of 3.8-, 5.33-, and 8.49-μm diameter as $3.6 + / - 0.90$, $5.0 + / - 1.2$, and $7.9 + / - 2.1$ μm (mean $+ / - 1$ standard deviation), respectively, Table 2. These results show a good diameter estimate accuracy (t-test, $\alpha = 0.05$) but with high probability of large (>25%) errors in individual measurements.

On OCT data from tissue sample 1 orientation 4, Fig. 7(a), the AR-SE technique predicted a heterogeneous distribution of fiber diameters in both fascicles, Fig. 7(b). A small difference between the scatterer diameter distributions in the left and right fascicles was predicted, with means of 7.6 and 8.1 μm, respectively, Table 2, and medians of 8.2 and 9.0, respectively, Fig. 7(c). The diameter distribution estimates were significantly different to those produced from the corresponding histology by light microscopy images (t-test, $\alpha = 0.05$; and Wilcoxon rank sum test, $\alpha = 0.05$), Fig. 7(c). Therefore, in the example analysis of this image, the AR-SE technique correctly predicted a larger scatterer diameter distribution in the right fascicle but did not accurately quantify the difference between the two fascicles' distributions.

3.2.3 *Correlation of the derivative spectral estimation technique*

The CoD technique estimated the diameters of microsphere samples of 3.8-, 5.33-, and 8.49-μm diameter as $2.6 + / - 0.7$,

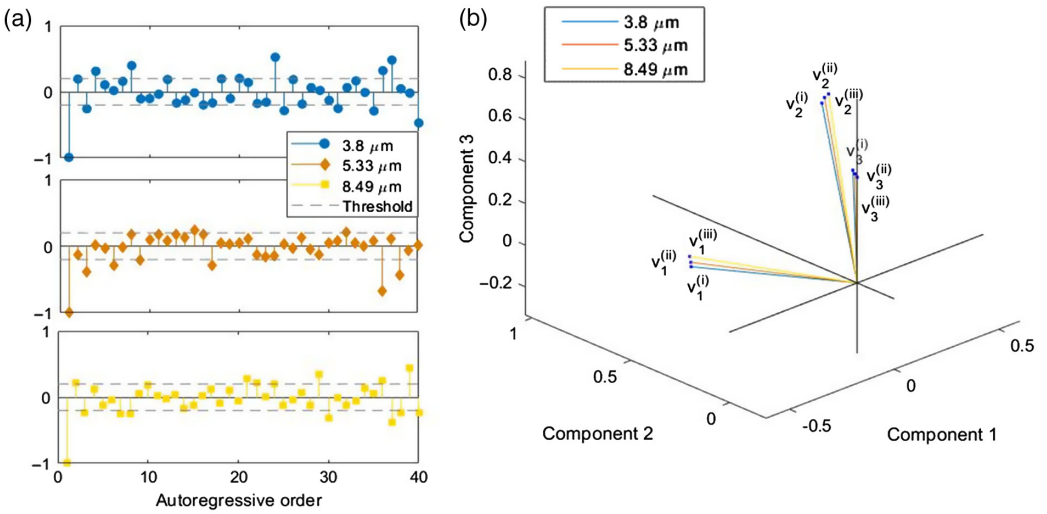

Fig. 6 (a) The first 40 autoregressive reflection coefficients, used to determine the autoregressive order when calculating the power spectral density, showing a rapid decay toward zero for all three the microsphere samples. (b) Contributions of the first three variables, v_1, v_2, and v_3, to the first three principal components, component 1, component 2, and component 3, from weighted PCA of the power spectral densities of (i) 3.8-, (ii) 5.33-, and (iii) 8.49-μm diameter microsphere samples.

Table 2 Scatterer diameter estimates, in μm, of microsphere samples and the intra-fascicle volume of the left and right fascicles in tissue sample 1 orientation 4. Estimates from histology, a 10×10 window in the AR-SE technique, the "CoD-SE: conventional" technique, which selects each estimate based on minimization of the standard deviation, and the "CoD: normalized s.d. technique, which selects each estimate based on minimization of the normalized standard deviation. Data are presented as mean (standard deviation) in μm.

	Manufacturer's data/histology (μm)	AR-SE (μm)	CoD-SE: conventional (μm)	CoD-SE: normalized s.d. (μm)
3.8-μm microspheres	3.8 (0.25)	3.6 (0.9)	4.3 (1.5)	4.3 (1.5)
5.33-μm microspheres	5.33 (0.25)	5.0 (1.2)	4.6 (1.5)	5.7 (1.4)
8.49-μm microspheres	8.49 (0.25)	7.9 (2.1)	6.3 (1.9)	6.3 (1.9)
Tissue sample 1 orientation 4				
Left fascicle	6.9 (2.2)	7.6 (4.8)	9.7 (3.3)	10.4 (4.4)
Right fascicle	10 (3.1)	8.1 (4.6)	9.6 (3.2)	10.9 (4.4)

$2.8 + / - 0.5$, and $4.5 + / - 0.3$ μm (mean $+ / -$ 1 standard deviation), respectively, which indicates poor diameter estimate accuracy for all microsphere diameters, Table 2. All estimates corresponded to a scanning window axial size of 4 pixels, selected to minimize the standard deviation, whereas the smallest window axial size used in the original study was 5 pixels,[21] Figs. 8(a)–8(c). Excluding window axial sizes of 3 and 4 pixels from consideration provided a significant improvement in estimate accuracy: $4.3 + / - 1.5$, $4.6 + / - 1.5$, and $6.3 + / - 1.9$ μm, respectively. For all microsphere samples, the magnitude of diameter estimates showed a decreasing trend with decreasing axial window size, as did the standard deviation of estimates, which results in smaller diameter estimates being favored. Selection via minimization of the normalized standard deviation removed the effect of the downward trends, and, with window axial sizes of 3 and 4 pixels excluded, increased the estimate for 5.33-μm microspheres to $5.7 + / - 1.4$ μm, Figs. 8(d)–8(f). Estimates for 3.8 and 8.49 μm microspheres remained unchanged, Table 2.

On OCT data of nerve tissue, pixels containing air produced an estimate of 1.775 μm, which corresponded to a lag of 1500(a.u.) and was the limit of considered range of the power fit to the theoretical CoD curve, Fig. 8(g). As mentioned earlier, in Sec. 3.1.4, epineurium produced estimates within the range of 2.2 to 4 μm. Therefore, to remove air and epineurium, scatterer diameter estimates of $\leq$4 μm were discarded in our analysis of fiber diameter distribution. On OCT data from tissue sample 1 orientation 4, Fig. 9(a), the CoD-SE algorithm predicted a heterogeneous distribution of fiber diameters in both the left and right fascicles, Fig. 9(b). A small difference between the scatterer diameter distributions in the left and right fascicles was predicted, with means of 10.4 and 10.9 μm, respectively, Table 2, and medians of 10.0 and 10.6 μm, respectively, Fig. 9(c). As for the AR-SE technique, the normalized

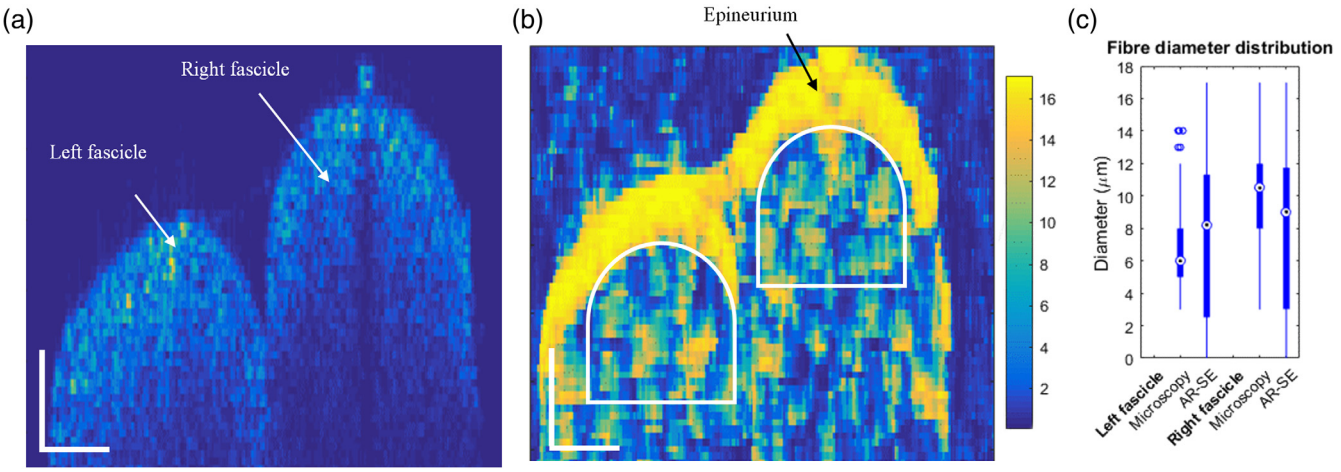

Fig. 7 (a) OCT data of tissue sample 1 orientation 4 and (b) the same image after processing with AR-SE technique, scale bars in (a) and (b) are 100 μm. In (b) the epineurium layer is visible as a contiguous layer of large diameter scatterers, with diameter on the color scale. The white outlined region in (b) indicate the areas where data were used to produce the fiber diameter distribution estimate with the CoD-SE algorithm for each fascicle, which are compared against the results from histology by light microscopy in a box and whisker plot (c). The AR-SE technique correctly predicted a larger scatterer diameter distribution in the right fascicle but did not accurately quantify the difference between two fascicles' distributions.

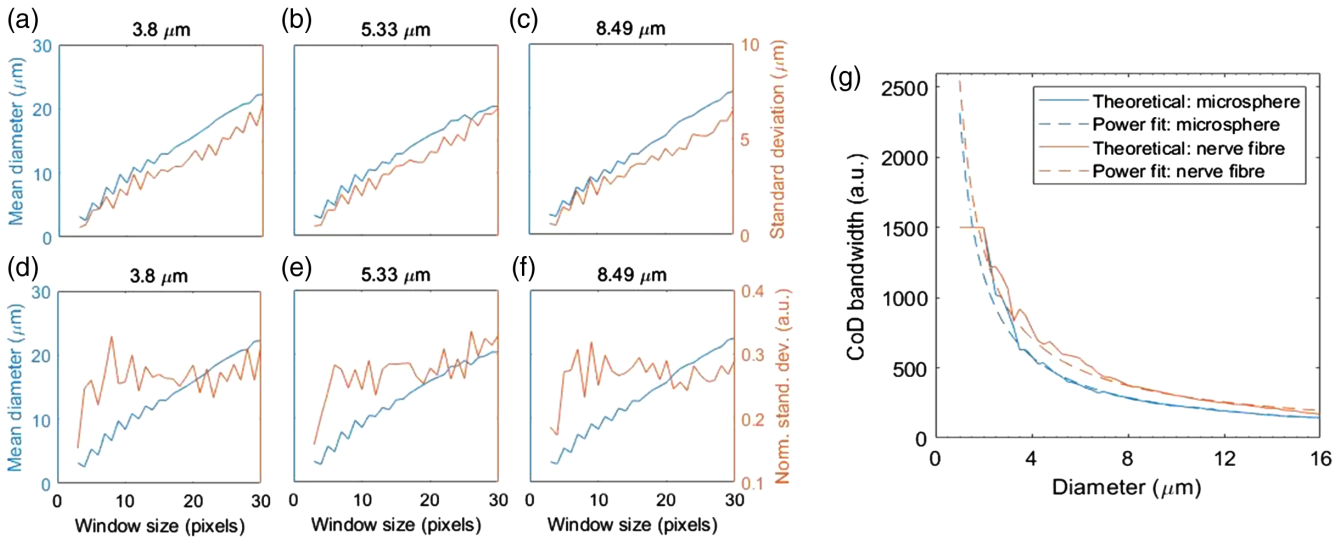

Fig. 8 (a–c) Mean and standard deviation, or (d–f) mean and normalized standard deviation, of diameter estimates produced by each window size on microsphere samples. (d–f) Normalizing the standard deviation, (a–c) removes the decreasing trend with window size which seen in standard deviations. The CoD bandwidth across the scatterer diameter range of 1 to 16 μm, generated using refractive indices of water and polystyrene for use with microsphere samples, and refractive indices of bovine tendon and myelin for use with peripheral nerve samples (g).

CoD-SE technique correctly predicted a larger mean scatterer diameter in the right fascicle, but did not accurately quantify the difference.

3.3 *Adipose Tissue Identification*

3.3.1 *Average depth-resolved profile technique*

Using the 5 A-scan sliding window method and calculating the threshold from the entire portion of the residual SNR curve, regions with adipose tissue apposed to the outer nerve boundary cross the threshold several times throughout the depth, Figs. 10(b) and 10(c). In contrast, regions with epineurium crossed the threshold only once Figs. 10(a) and 10(c). Thus, layers of adipose tissue were qualitatively distinguishable from epineurium tissue, a finding not reported in the original study.[18] Further studies on this effect are needed to establish the repeatability of this observation. It was not possible to identify the outer epineurium boundary beneath adipose tissue, and, as a result, the thickness of adipose tissue could not be estimated, nor was it possible to identify the uniformly decaying region indicating the intrafascicle volume beneath adipose tissue. The presence of adipose tissue, therefore, reduces the amount of information available from the ADRP technique.

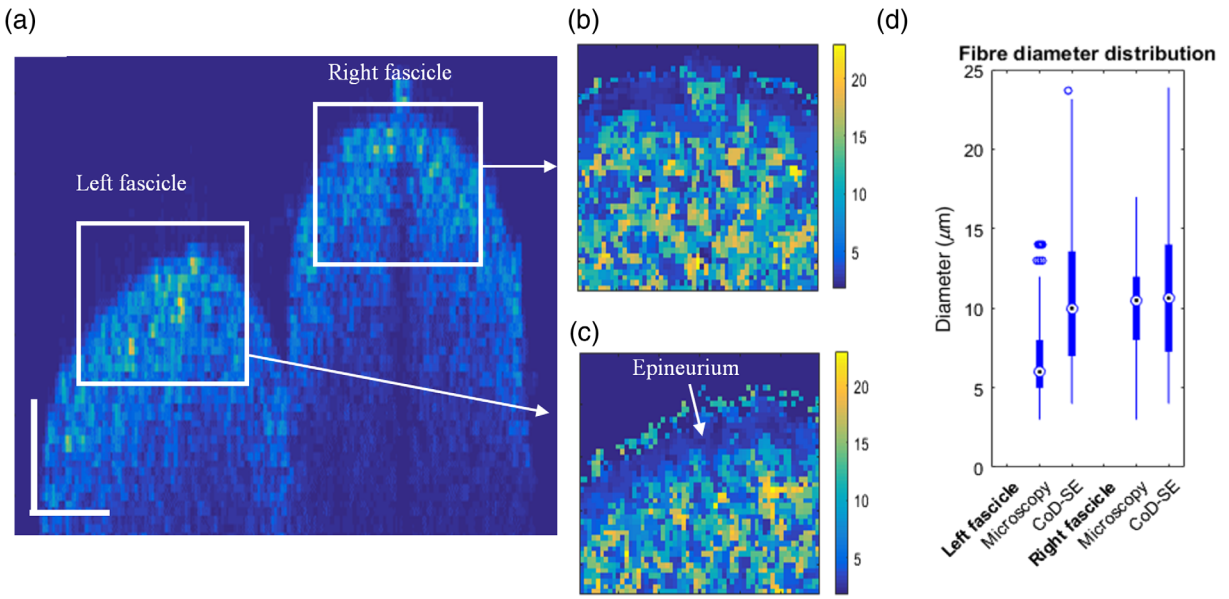

Fig. 9 OCT data of tissue sample 1 orientation 4 (a) with white boxes indicating the areas of the left and right fascicles used for analysis with the CoD-SE algorithm, and the white scale bar bottom left indicating 100 μm. The boxed areas in (a) are shown after processing with CoD-SE algorithm in (b) and (c), for the right and left fascicles, respectively, with diameter on a color scale. The diameter distribution of estimates within areas (b) and (c), with values below 4 μm excluded, are compared against results from histology by light microscopy in a box and whisker plot (d). The normalized CoD-SE technique correctly predicted a larger mean scatterer diameter in the right fascicle, but did not accurately quantify the difference.

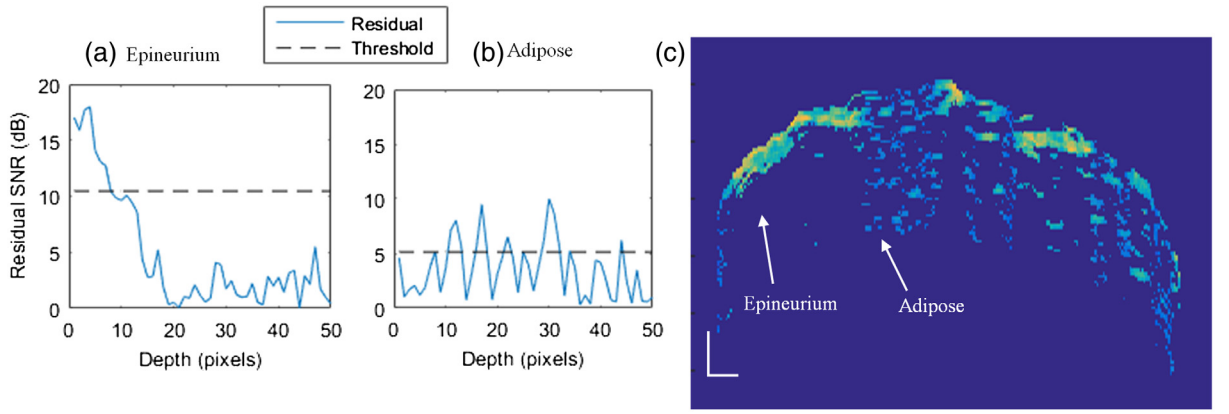

Fig. 10 Residual SNR curve of epineurium (a) is clearly distinguishable from adipose tissue (b) as the threshold, when calculated from the entire residual curve, intercepts with a single large peak. A color map of tissue sample 1 orientation 2 produced by the ADRP-five A-scan method showing only above-threshold residual SNR data (c) with white scale bar bottom left indicating 100 μm; a significant amount of adipose tissue is visible.

3.3.2 *Autoregressive spectral estimation technique*

Adipose tissue was qualitatively identified within the AR-SE technique as clusters of large diameter scatterers present in areas of the image, where the contiguous layer of scatterers on the nerve surface, characteristic of epineurium tissue, was absent. It was not possible to identify the boundary between epineurium and adjacent adipose tissue, and, as a result, the thickness of adipose tissue could not be estimated. A heterogeneous distribution of nerve fibers could feasibly also appear as clusters of large diameter scatterers. Thus, it was not possible to distinguish adipose tissue from the intrafascicle volume. Similarities between AR-SE estimates of adipose tissue, epineurium, and heterogeneous fiber diameter distribution meant that adipose tissue could not be identified with confidence without referencing against the corresponding light-microscopy images.

3.3.3 *Correlation of the derivative spectral estimation technique*

Adipose tissue appeared as a heterogeneous distribution of scatterers within the range of 2 to 19 μm. A method of distinguishing adipose tissue from intrafascicle volume was not found. The 50 μm and greater size of adipose cells, observed in histology by light microscopy, is beyond the Mie scattering range and so their true size cannot be estimated using the CoD-SE technique.

4 Discussion

A reference value for the combined thickness of epineurium and perineurium can be estimated by the summation of the epineurium thickness range in Ref. 8 of $47 +/- 25$ μm for Sprague–Dawley rats weighing 350 to 450 g, and the perineurium thickness range from Ref. 10 of 3 to 5 μm for Wistar rats weighing 200 to 250 g, producing a combined thickness of approximately $51 +/- 26$ μm. This reference value is in broad agreement with the values we obtained from histology, of $50 +/- 38$ μm, $45 +/- 32$ μm (mean $+/-$ 1 standard deviation) for tissue samples 1 and 2, respectively. The value for tissue sample 3, of $31 +/- 25$ μm, is not directly comparable as it is from the tibial, not the sciatic, branch. It is evident from the size of the standard deviations, which are large relative to mean values in both Ref. 8 and our estimates, that there is a significant variation in epineurium and perineurium tissue thickness across the cross section of each tissue sample. The standard deviations for epineurium thickness estimates obtained using light microscopy were less variable than those obtained using the ADRP and AR-SE techniques, Table 1, which we expect is due to the former being a direct measurement technique, whereas the latter two use more variables in their calculation.

When the ADRP was calculated using the middle 50% of A-scans, the technique produced estimates of epineurium thickness with an average of 86 μm, and which were consistently lower than those in the original paper,[18] which reported an average thickness of 133 μm on sciatic nerve of Sprague–Dawley rats. Both of these values, 86 and 133 μm, are significantly above our reference value of $51 +/- 26$ μm.[8,10] In addition, all of the epineurium thickness estimates we produced using this technique were consistently and significantly larger than the corresponding estimates using histology by light microscopy. The technique, therefore, appears to consistently and significantly overestimate the epineurium thickness. The accuracy of epineurium thickness estimates using the ADRP technique were significantly improved through the addition to the method of a scanning window containing five adjacent A-scans. The 5 A-scan ADRP technique also resolves the image with a higher transverse resolution, which is beneficial to practical application of the technique due to the variable epineurium thickness observed in the histology by light microscopy. A qualitative method of identifying adipose tissue through the residual SNR is a new application of the ADRP technique. However, further studies are required to evaluate the repeatability of the proposed method.

Use of the structural and optical differences within the peripheral nerve to estimate epineurium layer thickness is an application of scatterer diameter estimation techniques, such as AR-SE and CoD. In the AR-SE technique, our observation of epineurium as a contiguous layer of large diameter scatterers presents a new means to identify the epineurium boundary. Our initial results of thickness estimates, using the difference between the full width half mean of the contiguous scatterer peak and the axial scanning window size, are very promising. However, the accuracy of thickness estimates was significantly reduced by the inability of the technique to distinguish between the tissue layer and large diameter nerve fibers apposed to the inner tissue boundary, which, accordingly, inflates the affected tissue thickness estimates. In addition, the tendency of the AR-SE algorithm to produce some thickness estimates of 0 μm, which is biologically impossible, raises the question of robustness of using the full width half mean of the contiguous scatterer peak as an estimate of the base-width. Further studies on the relationship between the contiguous scatterer layer and epineurium thickness are needed.

In the CoD-SE technique, the epineurium tissue layers were visually identified as a contiguous layer of scatterers; however, a method to isolate this layer and a quantitative method to analyze the thickness were not identified in the current study. Application of the CoD-SE technique to estimating epineurium thickness from the contiguous layer is expected to suffer from the same problem identified in the AR-SE technique: an inability to distinguish epineurium tissue from clusters of fibers adjacent to the internal tissue boundary. This inability appears to be an inherent shortfall in the application of scatterer diameter estimation techniques to distinguishing tissue layers.

Differences in fiber diameter distribution between fascicles were correctly identified by both the AR-SE and normalized CoD-SE techniques, however, the magnitude of this difference was not estimated accurately by either technique. In the AR-SE technique, we postulate that the estimate accuracy may be improved through the use of more biomimetic samples to populate the coefficient matrix within the algorithm. However, producing samples that mimic densely packed nerve fibers within the intra fascicle volume using materials with comparable refractive indices poses a challenge. Alternatively, spectral data gathered from fascicles of known fiber diameter distribution could be used to train the algorithm. Conversely, because the CoD-SE technique uses a Mie theory-based model to predict the spectra, the challenge lies in locating suitable values for the refractive indices of the biological tissue and cellular layers. Furthermore, the myelinated fiber contains an internal scattering boundary between the myelin sheath and intracellular fluid of the axon which has not been considered in the current study.

In all techniques, inaccuracy was compounded by the low axial resolution of our OCT system (10 μm in air) relative to the lower bounds of epineurium tissue layer thickness (10 μm) present in some areas of each tissue sample. None of the techniques could identify the epineurium boundaries beneath adipose tissue or on the far side of the intrafascicle volume. Therefore, application of the techniques appears to be limited in depth, perhaps to as little as the first 100 to 200 μm, due to limitations of the techniques and to the highly scattering nature of adipose tissue and nerve fibers. This is in broad agreement with an observation by authors of the original ADRP technique,[18] performed on an OCT system with 11-μm axial resolution in air, that the ADRP technique is unreliable at >300 μm depth due to a decrease in the SNR. The authors of the original AR-SE technique, performed on an OCT system with 13-μm axial resolution in air, qualitatively implied the presence of three fascicles within an OCT image of a peripheral nerve at depths of up to 500 μm,[19] although, as the authors point out, without any validation. Several 100's of μm depth penetration is sufficient to image the minor branches of the major nerves in humans, such as the pronator teres, flexor carpi radialis, and digital branches of the median nerve.[9] Furthermore, some medical applications, such neural tissue identification as an aid to surgery,[11] do not require significant depth penetration, whereas others, such as monitoring of epineurium thickness in response implantation of nerve-cuff electrodes,[34] or monitoring of myelination post crush injury,[17] may garner useful information from the outer layers of the nerve alone.

The principal advantage of OCT in extracting morphometric information from peripheral nerve is the wealth of information present in the OCT signal. As was the case in the current study, several signal processing techniques can be applied to a single set of OCT data, obtained from each nerve, to extract multiple morphometric details such as epineurium thickness (ADRP and AR-SE techniques), fiber diameter distribution (AR-SE and CoD techniques), and tissue classification (ADRP technique). Variation of morphometric details along the length of the nerve could then be easily accomplished using C-scans.

5 Conclusion

Three OCT signal analysis techniques were evaluated and improved upon in this study as a means to extract morphometric details of peripheral nerves. New methods of estimating the epineurium thickness were identified, and the initial accuracy of results is promising. Further development of these techniques and the use of higher resolution OCT system are expected to improve the accuracy. Methods of quantifying the fiber diameter distribution were not successfully produced; however, factors that potentially improve the methods were identified. This study has characterized some of the abilities and limitations of OCT in extracting morphometric information of peripheral nerve and identified future research directions in this area.

Disclosures

The authors have no relevant financial interests in this article and no potential conflicts of interest to disclose.

References

1. P. Garai et al., "Influence of anatomical detail and tissue conductivity variations in simulations of multi-contact nerve cuff recordings," *IEEE Trans. Neural Syst. Rehabil. Eng.* **25**(9), 1653–1662 (2017).
2. Y. Grinberg et al., "Fascicular perineurium thickness, size, and position affect model predictions of neural excitation," *IEEE Trans. Neural Syst. Rehabil. Eng.* **16**(6), 572–581 (2008).
3. K. E. I. Deurloo, J. Holsheimer, and P. Bergveld, "Fascicular selectivity in transverse stimulation with a nerve cuff electrode: a theoretical approach," *Neuromodulation* **6**(4), 258–269 (2003).
4. A. Q. Choi, J. K. Cavanaugh, and D. M. Durand, "Selectivity of multiple-contact nerve cuff electrodes: a simulation analysis," *IEEE Trans. Biomed. Eng.* **48**(2), 165–172 (2001).
5. C. R. Butson et al., "Selective neural activation in a histologically derived model of peripheral nerve," *J. Neural Eng.* **8**(3), 036009 (2011).
6. M. A. Schiefer, R. J. Triolo, and D. J. Tyler, "A model of selective activation of the femoral nerve with a flat interface nerve electrode for a lower extremity neuroprosthesis," *IEEE Trans. Neural Syst. Rehabil. Eng.* **16**(2), 195–204 (2008).
7. S. Sunderland and F. Walshe, *Nerves and Nerve Injuries*, Williams and Wilkins Co., Baltimore (1968).
8. G. A. Dumanian, M. A. McClinton, and T. M. Brushart, "The effects of free fat grafts on the stiffness of the rat sciatic nerve and perineural scar," *J. Hand Surg.* **24**(1), 30–36 (1999).
9. I. Delgado-Martínez et al., "Fascicular topography of the human median nerve for neuroprosthetic surgery," *Front. Neurosci.* **10**, 286 (2016).
10. B. Layton and A. Sastry, "A mechanical model for collagen fibril load sharing in peripheral nerve of diabetic and nondiabetic rats," *J. Biomech. Eng.* **126**(6), 803–814 (2004).
11. M. E. Brezinski et al., "Optical biopsy with optical coherence tomography: feasibility for surgical diagnostics," *J. Surg. Res.* **71**(1), 32–40 (1997).
12. N. M. Fried et al., "Imaging the cavernous nerves in the rat prostate using optical coherence tomography," *Lasers Surg. Med.* **39**(1), 36–41 (2007).
13. M. Aron et al., "Second prize: preliminary experience with the Niris™ optical coherence tomography system during laparoscopic and robotic prostatectomy," *J. Endourol.* **21**(8), 814–818 (2007).
14. Y. Yoon et al., "Visualization of prostatic nerves using polarization-sensitive optical coherence tomography," in *11th Conf. on Lasers and Electro-Optics Pacific Rim (CLEO-PR)* (2016).
15. C.-T. Chang et al., "Finite element modeling of hyper-viscoelasticity of peripheral nerve ultrastructures," *J. Biomech.* **48**(10), 1982–1987 (2015).
16. C. A. Chlebicki et al., "Preliminary investigation on use of high-resolution optical coherence tomography to monitor injury and repair in the rat sciatic nerve," *Lasers Surg. Med.* **42**(4), 306–312 (2010).
17. F. P. Henry et al., "In vivo optical microscopy of peripheral nerve myelination with polarization sensitive-optical coherence tomography," *J. Biomed. Opt.* **20**(4), 046002 (2015).
18. M. S. Islam et al., "Extracting structural features of rat sciatic nerve using polarization-sensitive spectral domain optical coherence tomography," *J. Biomed. Opt.* **17**(5), 056012 (2012).
19. A. Kartakoullis, E. Bousi, and C. Pitris, "Scatterer size-based analysis of optical coherence tomography images using spectral estimation techniques," *Opt. Express* **18**(9), 9181–9191 (2010).
20. E. Bousi, A. Kartakoullis, and C. Pitris, "Spectral analysis for scatterer estimation in optical coherence tomography images," in *Final Program and Abstract Book—9th Int. Conf. on Information Technology and Applications in Biomedicine*, ITAB (2009).
21. M. Kassinopoulos et al., "Correlation of the derivative as a robust estimator of scatterer size in optical coherence tomography (OCT)," *Biomed. Opt. Express* **8**(3), 1598–1606 (2017).
22. D. Levitz et al., "Determination of optical scattering properties of highly-scattering media in optical coherence tomography images," *Opt. Express* **12**(2), 249–259 (2004).
23. J. Hope et al., "Extracting morphometric information from rat sciatic nerve using optical coherence tomography (OCT)—review and comparison of methods," in *Australian New Zealand Conf. on Optics (ANZCOP)*, Queenstown, New Zealand (2017).
24. M. Kassinopoulos and C. Pitris, "Development of a new, robust and accurate, spectroscopic metric for scatterer size estimation in optical coherence tomography (OCT) images," *Proc. SPIE* **9697**, 96971V (2016).
25. G. Liu et al., "Stress and strain analysis on the anastomosis site sutured with either epineurial or perineurial sutures after simulation of sciatic nerve injury," *Neural Regener. Res.* **7**(29), 2299–2304 (2012).
26. M. Goodwin et al., "Polarisation-sensitive optical coherence tomography as a method for quantifying cartilage degeneration in the Bovine model," in *European Conf. on Biomedical Optics*, Munich, Germany, p. EW3A.36 (2017).
27. B. Brauer et al., "Simple and inexpensive long range swept source for optical coherence tomography applications," in *SPIE-BIOS*, San Fransisco, California, paper 9312–125 (2015).
28. J. B. Arous et al., "Single myelin fiber imaging in living rodents without labeling by deep optical coherence microscopy," *J. Biomed. Opt.* **16**(11), 116012 (2011).
29. D. Maciel et al., "Quantitative phase measurements of tendon collagen fibres," *J. Biophotonics* **10**(1), 111–117 (2017).
30. A. Kartakoulis and C. Pitris, "Scatterer size-based analysis of optical coherence tomography signals," *Proc. SPIE* **6627**, 66270N (2007).
31. C. Mätzler, "MATLAB functions for Mie scattering and absorption, version 2," IAP Res. Rep. 8, pp. 1–24 (2002).
32. C. Mätzler, "MATLAB functions for Mie scattering and absorption," Research Report, Institute of Applied Physics, University of Bern (2002).
33. X. Ma et al., "Determination of complex refractive index of polystyrene microspheres from 370 to 1610 nm," *Phys. Med. Biol.* **48**(24), 4165–4172 (2003).
34. M.-A. Thil, I. M. Colin, and J. Delbeke, "Time course of tissue remodelling and electrophysiology in the rat sciatic nerve after spiral cuff electrode implantation," *J. Neuroimmunol.* **185**(1), 103–114 (2007).

James Hope is a doctoral candidate at the University of Auckland, from where he gained his BE(hons) degree and then his MEngSt degree in medical devices and technologies with first class honours.

His research interests are neural prosthetics, orthotics, and smart materials.

Bastian Braeuer gained his PhD in physics from the University of Auckland. His doctoral thesis, "Source development and dispersion measurements in optical coherence tomography," involved developing dual band OCT systems to measure and characterize dispersion in intraocular fluid.

Satya Amirapu is the faculty histologist and a medical laboratory scientist at the University of Auckland. She is experienced in histotechnology, histology and histopathology for over 30 years.

Andrew McDaid is a senior lecturer at the University of Auckland. He gained his BE degree with first class honours and his PhD from the University of Auckland in 2008 and 2012, respectively. He is a multidisciplinary researcher with expertise in mechatronics engineering, smart materials, and control systems. His main research interests are developing intelligent medical robotics devices for people who have suffered injury, stroke, or have disabilities.

Frédérique Vanholsbeeck is a senior lecturer and head of the Bio-Photonics Group at the University of Auckland, and a principal investigator at the Dodd Walls Centre for Photonic and Quantum Technologies. Her research focuses are an all-fibre real-time spectroscopic optical probe (or optrode), medical applications of OCT imaging, and nonlinear imaging.